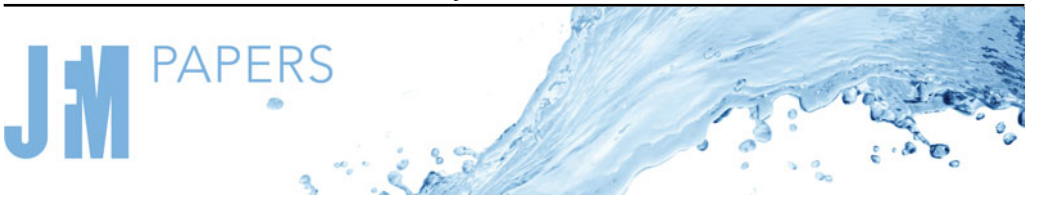
J. Fluid Mech. (2025), *vol.* 1013, A2, doi:10.1017/jfm.2025.10207



Rebounding hydrogel sphere water entry

Xiaoyan Ye[1], **Kaizhao Qin**[1], **Rui Yang**[2] **and Joshua A. Dijksman**[3]

[1]Key Laboratory of Mechanics on Disaster and Environment in Western China attached to the Ministry of Education of China, and Department of Mechanics and Engineering Science, School of Civil Engineering and Mechanics, Lanzhou University, Lanzhou, Gansu 730000, PR China

[2]Department of Mechanical and Aerospace Engineering, Princeton University, Princeton, NJ 08544, USA

[3]Van der Waals-Zeeman Institute, Institute of Physics, University of Amsterdam, Science Park 904, 1098 XH Amsterdam, The Netherlands

Corresponding author: Xiaoyan Ye, yexy@lzu.edu.cn

(Received 15 November 2024; revised 31 March 2025; accepted 18 April 2025)

The interaction between elastic structures and fluid interfaces, known as 'hydroelastic' problems, presents unique challenges to classical frameworks established for rigid spheres and liquid droplets. In this work, we experimentally demonstrate an intriguing phenomenon where ultrasoft hydrogel spheres rebound from a water surface at high impact speeds, even when their density exceeds that of water. We further propose a theoretical force-balance model, incorporating energy redistribution and potential flow theory, to predict the critical impact speed for the transition from sinking to rebounding, as well as the temporal evolution of both spreading diameter and cavity expansion. Our findings extend the classical Weber- and Bond-number-dominated paradigms for rigid spheres and liquid droplets, demonstrating that hydrogel dynamics is controlled by a modified elastocapillary Mach number, with rebound achievable even for hydrophilic spheres. These findings improve the understanding of soft-impact hydrodynamics and offer design principles for applications in biomimetic robotics and energy-absorbing materials.

Key words: flow-structure interactions, drops and bubbles, viscoelasticity

1. Introduction

Water entry problems, a phenomenon studied for centuries, have been motivated by a wide range of interests, from the ancient art of stone skipping to naval applications, water-surface craft (Halswell *et al.* 2012) and the biological/biomimetic dynamics of water-walking (Richardson 1948; Glasheen & McMahon 1996; Bush & Hu 2006; Kubota *et al.* 2015), as well as impacts on granular flows (Lohse *et al.* 2004; Zhao, de Jong & van der Meer 2019; Ye & Meer 2021). Classical studies of rigid-sphere impact have demonstrated a complex interplay between projectile dynamics and cavity evolution.

© The Author(s), 2025. Published by Cambridge University Press.

https://doi.org/10.1017/jfm.2025.10207 Published online by Cambridge University Press

According to Aristoff & Bush (2009) and Speirs *et al.* (2019) and other related work (Korobkin & Pukhnachov 1988; Truscott, Epps & Belden 2014), the accurate modelling of these phenomena may be characterised by five dimensionless numbers: Weber number $We = \rho_w U_0^2 R_0/\sigma$, Bond number $Bo = \rho_w g R_0^2/\sigma$, Reynolds number $Re = \rho_w U_0 R_0/\eta$, solid–liquid density ratio $\rho = \rho_s/\rho_w$ and air–liquid density ratio $\tilde{\rho} = \rho_a/\rho_w$, where ρ_s is the sphere density and R_0 is the radius, σ is the surface tension, η is the dynamic viscosity of the liquid, ρ_w is the liquid density, ρ_a is the air density and g is the gravitational acceleration.

There are two distinct dynamical regimes governed by the Weber number. In the capillary-dominated regime ($We \leqslant 1$), surface tension enables dense spheres ($\rho \geqslant 1$) to establish a transient contact line and rebound through capillary forces (Vella, Lee & Kim 2006; Vella & Metcalfe 2007). Conversely, in the inertia-dominated regime ($We \gg 1$), cavity dynamics is controlled by the Froude number $Fr = U_0^2/(g D_0)$, with aerodynamic effects becoming negligible when $Fr \gg 1$ (Lee & Kim 2008; Truscott *et al.* 2014). In this regime, whether the rigid sphere rebounds during impact depends on two characteristic time scales: the cavity collapse time τ_p and the sphere deceleration time τ_c. Following Duclaux *et al.* (2007), τ_p represents the cavity pinch-off time. When $\tau_c \gg \tau_p$, the sphere's motion decouples from cavity evolution as deceleration becomes insignificant during collapse. While when $\tau_c \approx \tau_p$ (Aristoff *et al.* 2010), the coupled interaction between sphere dynamics and cavity evolution enables rebound through synchronised fluid–structure interactions.

Key advancements in rigid sphere rebounds, as demonstrated by Aristoff *et al.* (2010), revealed that low-density rigid spheres ($\rho < 0.3$) with a contact angle of approximately 120° experience upward forces due to cavity collapse. Further research by Lee & Kim (2008) found that hydrophobic rigid spheres with a contact angle of 154° and $\rho \approx 1$ exhibit rebound when $We Bo^{3/2} \approx 8$, where $Bo \approx 5$ and $We \leqslant 2$. Additionally, the study by Speirs *et al.* (2019) extended the range of contact angles of the spheres from 84° to 145°, revealing that spheres rebound at $We < 1$ and $Bo < 0.5$.

Correspondingly, the cavity behaviour can be classified into four distinct categories – quasi-static, shallow seal, deep seal and surface seal – depending on Bo and We (Aristoff & Bush 2009). It is worth noting that Duclaux *et al.* (2007) provided an analytical solution for cavity evolution, assuming that the sphere does not influence the cavity. This suggests that the cavity evolution follows a scaling of $t^{1/2}$, according to potential flow theory, and this relationship is also observed when considering the interaction between the sphere and the cavity. Aristoff & Bush (2009) further developed a more specific theoretical framework to characterise the evolving cavity dynamics, accounting for the effects of rigid-sphere velocities.

Regarding droplet–liquid impact, there are four distinct regimes of droplet behaviour (Zhao, Brunsvold & Munkejord 2011): low-energy collision coalescence, bouncing, high-energy collision coalescence and splashing. These regimes are characterised by a sequence of interfacial phenomena, such as transient crown formation, air entrainment cavity dynamics and subsurface bubble generation, all of which are governed by the dimensionless parameters, particularly We, Re and Ohnesorge number (Gilet & Bush 2012; Lhuissier *et al.* 2013). The rebound phenomenon is particularly sensitive to interfacial physics, requiring a precise balance of competing forces. As demonstrated in Richard & Quéré (2000), droplet bouncing on thin liquid films necessitates sustained air cushioning, with rebound occurring only when inertial forces balance the retention of interfacial energy. Hydrophobic surfaces amplify droplet rebound behaviour(Tran *et al.* 2013) and enable complete droplet ejection from the liquid, a phenomenon known as

https://doi.org/10.1017/jfm.2025.10207 Published online by Cambridge University Press

hydrodynamic bouncing (Korobkin & Pukhnachov 1988; Lee & Kim 2008; Truscott *et al.* 2014).

While the dynamics of rigid solids and liquid droplets during water impact is well characterised (Bush & Hu 2006), hydrogels – due to their high water content, strong hydrophilic properties and viscoelastic features – exhibit mechanisms of transition from rigid to liquid impact behaviour in granular media (Ye & Meer 2021). Unlike rigid spheres or liquids, hydrogel spheres undergo significant deformation upon impact, storing elastic energy, altering cavity dynamics and leading to unexpected behaviours by fluid–structure coupling. Experimental and theoretical studies (Hurd *et al.* 2017) on the vertical water entry of elastic spheres demonstrate that deformations of the sphere induce wavy disturbances in the cavity. Furthermore, Belden *et al.* (2016) performed experiments and numerical simulations of elastic spheres during oblique water entry, revealing that elastic spheres exhibit superior water-skipping ability compared with rigid spheres. This is attributed to the deformation of the sphere, which is governed by the elastic Mach number $Ma = U_0/U_e$. Besides, deformable spheres can achieve skipping at an impact angle of $\beta = 47°$ when $\rho = 0.959$ (Belden *et al.* 2016), which exceeds the upper limit of $\beta = 18°/\sqrt{\rho}$ (Richardson 1948) for rigid spheres. In vertical impact experiments, Rabbi *et al.* (2022) investigated soft hydrogel spheres impacting a droplet and observed a bouncing phenomenon. They identified a modified elastic Mach number V_e/U_e, where V_e is the spreading velocity of the droplet, to determine the onset of droplet lift-off.

Therefore, deformable hydrogel spheres present a unique feature for investigating fluid–structure interactions during water entry. Here, an experiment for hydrogel spheres vertically impacting into liquid is performed. We measure sphere deformation and cavity dynamics during impact using high-speed cameras, examining how the motion of spheres depends on control parameters through energy distribution and potential flow theory. An analytical model relates the maximum deformation area and velocity to hydrodynamic drag, identifying rebound mechanisms and predicting parameter ranges for rebound. This approach can also be applied to other natural systems like basilisk lizards and shorebirds, which exploit inertial forces by hyperextending limbs to conform to transient cavities, followed by energy recovery during rebound (Glasheen & McMahon 1996; Kubota *et al.* 2015).

The paper is structured as follows: In § 2, we discuss the experimental set-up, the production of the hydrogel sphere and the measurement method of Young's modulus, as well as the preparation of liquids with varying viscosities. In § 3, we exhibit the motion of the hydrogel spheres and the evolution of the cavity. Section 4 then focuses on the decomposition of the impact kinetic energy E_k into two components: the energy used for the deformation of the sphere (E_d) and the energy contributed to the formation of the cavity (E_s). Finally, in § 5, we investigate the bouncing phenomenon, exploring the conditions under which the spheres rebound and analysing the process in terms of time scales. The paper is concluded in § 6.

2. Experimental methods

We investigate how varying the impact velocity U_0, the stiffness characterised by Young's modulus Y of the spheres and the viscosity of liquid influence the entry of deformable hydrogel spheres into liquids. The experimental set-up is shown in figure 1(*a*), where two high-speed cameras at 10 000 frames per second are simultaneously employed to capture hydrogel sphere deformation and cavity profile at impact speeds U_0 ranging from 1 to 4.5 m s^{-1}. For instance, figures 1(*b*) and 1(*c*) are snapshots when the hydrogel sphere reaches its maximum diameter d_m and the corresponding cavity radius, respectively.

https://doi.org/10.1017/jfm.2025.10207 Published online by Cambridge University Press

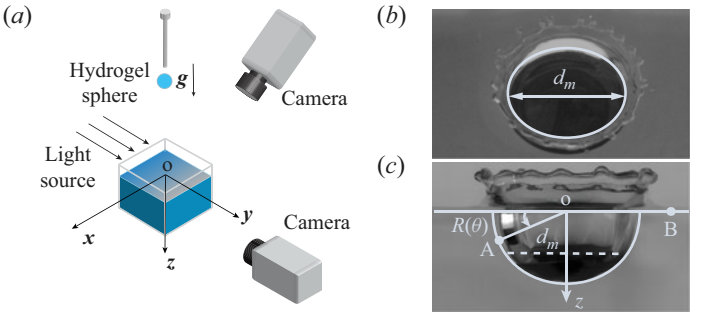


Figure 1. (*a*) Sketch of the experimental set-up. The impact of the hydrogel sphere and its deformation are imaged with one high-speed camera, whereas simultaneously, the cavity formation of the liquid is recorded by the second high-speed camera. (*b*) The moment when the diameter reaches its maximum d_m and (*c*) the cavity radius $R(\theta)$ at this instant.

A series of acrylamide gels are prepared by copolymerising acrylamide (40 % stock solution, Sigma-Aldrich) as the monomer and methylene bisacrylamide (2 % stock solution, Sigma-Aldrich) as the comonomer. To initiate and accelerate radical polymerisation, sodium persulphate (0.93 $\mathrm{g\,l^{-1}}$, Sigma-Aldrich) and tetramethylenediamine (0.6 $\mathrm{g\,l^{-1}}$, Sigma-Aldrich) were added. The monomer and comonomer solutions were premixed before the addition of initiators. Subsequently, a volume of 33.6 to 113.1 µl of this solution (corresponding to a hydrogel sphere with a diameter D_0 of approximately 4.0 to 6.0 mm) was transferred into an Eppendorf tube filled with polyoil of density 1.006 $\mathrm{g\,ml^{-1}}$ (Sigma-Aldrich) at 25 °C to match the solution's density, promoting polymerisation.

The polyacrylamide hydrogel sphere exhibits a static contact angle of 20.6° (Wu & Shanks 2004), indicating strong hydrophilicity. Meanwhile, Y of the hydrogel sphere was adjusted by varying the concentrations of the monomer and comonomer, which was evaluated using the Hertz theory for the deformation of an elastic sphere (Ye & Meer 2021):

$$F(\delta) = \frac{4Y}{3\sqrt{2}(1-\nu_P^2)} D_0^{1/2} \delta^{3/2}\,, \tag{2.1}$$

where Poisson's ratio $\nu_P = 0.5$ was determined by the incompressibility condition. The homemade set-up used for measuring Young's modulus comprises a scale and a micrometer, as illustrated in figure 2(*a*). A hydrogel sphere was placed between the scale and a rigid plate connected to a micrometer mounted on a stand. By adjusting the micrometer to apply quasi-static loading, the indentation δ of the sphere and the corresponding force F were recorded, as shown in figure 2(*b*). The measured Y ranges from approximately 50 to 1000 Pa, following the expected power law, as detailed in table 1.

We prepared liquid pools with controlled viscosity using ultrapure water and glycerol–water mixtures. The glycerol (Sigma-Aldrich, 99.5 % purity) was blended at various volume concentrations to produce solutions of specified viscosity, with detailed formulations listed in table 2. The density of each solution was measured experimentally, while viscosity and surface tension values were taken from the established work of Takamura, Fischer & Morrow (2012). These reference values show excellent agreement with both theoretical calculations (Cheng 2008; Chantelot *et al.* 2018) and independent experimental measurements (Sharma *et al.* 2020).

Before performing impact experiments, hydrogel spheres are suspended from a small nozzle connected to a vacuum pump that generates suction pressure. When the suction

https://doi.org/10.1017/jfm.2025.10207 Published online by Cambridge University Press

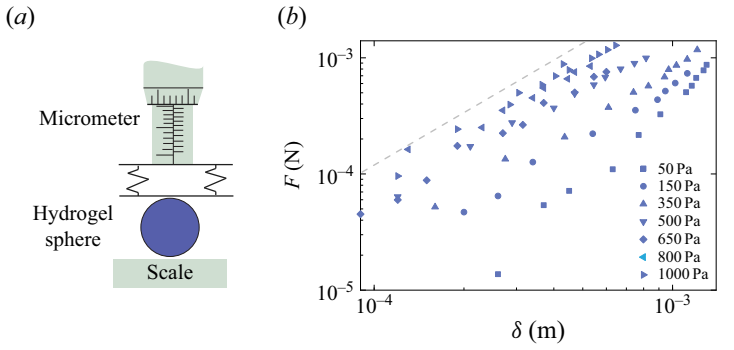


Figure 2. (*a*) The set-up for Young's modulus measurement. Hydrogel spheres were placed on a scale and a rigid plate, with the micrometer mounted on top of the plate. (*b*) Experimental data for hydrogel spheres with different moduli, where the dashed line represents the scaling with an exponent of 3/2, as predicted by Hertz theory. Note that the symbol legend of (*b*) is shared by the other figures.

Acrylamide (µl) (40 % stock solution)	Bisacrylamide (µl) (2 % stock solution)	Water (µl)	Density (kg m^{-3})	Y (Pa)	ΔY (Pa)
362	46.5	4591.5	1001	50	±8
375	75	4550	1001	150	±22
375	110	4515	1001	350	±10
375	125	4500	1001	500	±20
375	150	4475	1001	650	±32
375	200	4425	1001	800	±40
375	250	4375	1001	1000	±56

Table 1. Young's modulus Y of hydrogel spheres determined after polymerisation of different concentrations of acrylamide and bisacrylamide. Here, ΔY represents the standard deviation in Y, obtained from different batches of hydrogel spheres prepared using the same method.

Glycerol concentration (%)	Temperature (°C)	Density (ρ_w) (kg m^{-3})	Viscosity (η) (10^{-3} Pa s)
0	19	998	1.065
34	19	1076	3.369
50	19	1113	6.602
65	19	1194	17.092
80	19	1261	76.801

Table 2. Viscosity and other properties of ultrapure water and glycerol solution with different concentrations.

pressure was released, the spheres fell down vertically into a 10 cm × 10 cm × 8 cm liquid container under gravitational acceleration. It was checked that the boundaries of the container have a negligible effect on the impact results. We mainly focus on results obtained with the liquid viscosity η ranging from 1.065×10^{-3} to 76.801×10^{-3} Pa s at 19 °C, with dimensionless parameters spanning $We = 10$–10^3, $Bo = 1$–10 and $Re = 10^2$–10^4 (table 3). For comparison, we include parameter ranges from representative studies on rigid-sphere entry to liquid-surface rebound phenomena. The elastocapillary

https://doi.org/10.1017/jfm.2025.10207 Published online by Cambridge University Press

https://doi.org/10.1017/jfm.2025.10207 Published online by Cambridge University Press

Ref.	Weber number $We = \rho U_0^2 R_0/\sigma$	Bond number $Bo = \rho g R_0^2/\sigma$	Reynolds number $Re = \rho U_0 R_0/\eta$	Froude number $F = U_0^2/gR$	Density ratio ρ_s/ρ_w	Elastocapillary Mach number $Me = U_0/U_{ec}$	Contact angle θ	Remarks
Aristoff & Bush (2009); hydrophobic sphere	$10^{-1}-10^{3}$	$10^{-2}-10$	$10^{2}-10^{4}$	$10-10^{3}$	7.8		115°−125°	Cavity profile: $R(t) = (5/2)t\sqrt{\alpha}(U(z)/U_0)+1)^{2/5} \sim t^{2/5}$ At low B, the cavity type transitions from quasi-static to shallow seal to deep seal to finally surface sea as W is increased
Aristoff *et al.* (2010); hydrophobic sphere	$10-10^{3}$		$10^{3}-10^{5}$	$10-10^{2}$	0.2–7.8		115°−125°	Predict the pinch-off depth and time: $R(t,z) = \sqrt{-(z/F)t^2 + 2\sqrt{\alpha}Ut + 1}$
Duclaux *et al.* (2007); hydrophobic/ hydrophilic spheres/cylinder	$10^{2}-10^{3}$	$10^{3}-10^{4}$		$10-10^{2}$	2.5		Hydrophilic, hydrophobic	Spherical cavity collapses: $R(t) \sim ((2/3)(p_\infty/\rho R_0^3)^{1/5}(\tau - t)^{2/5}$ Cylindrical cavity: $R(t) \sim ((4R_0^2 p_\infty)/\rho)^{1/4}\sqrt{(\tau_0 - t)}$
Speirs *et al.* (2019); hydrophobic sphere	$10^{-1}-10^{4}$	$10^{-1}-10^{2}$		$1-10^{4}$	7.8		86°−144°	Cavity formation is dependent on the formation and behaviour of the splash crown. Three crown behaviours exist
Vella & Metcalfe (2007); hydrophobic cylinder	$10^{-1}-1$		10^{2}	1	0–4		72°−180°	There is a critical weight per unit length above which the line mass will sink
Lee & Kim (2008); hydrophobic sphere	$10^{-3}-10^{-2}$	$10^{-2}-10^{-1}$	$10^{2}-10^{3}$	$10-10^{2}$	0.9–2.25		154°	Boundary between oscillation and bouncing: $WeBo^{3/2} = 6/D_0^2$; boundary between bouncing and sinking: $WeBo^{3/2} = 12/D_0^2$
Zhao *et al.* (2011); drop	1−10	$10^{-4}-10^{-2}$	$10-10^{4}$	$10^{2}-10^{5}$	0.8–1		0°	Rebounding when $We < 10^1$; partial coalescence when $We < 10^1$; coalescence when $We < 10^1$
Hurd *et al.* (2017); elastic sphere	$10^{3}-10^{4}$	$10^{3}-10^{4}$	10^{5}	$10^{-1}-10$	1	0−10	Dragon skin	Sphere deceleration over the first deformation period: $\Delta U/U_0 \approx (G_\infty/\rho_w U_0^2)^{-1/2}$
Belden *et al.* (2016); elastic sphere	$10-10^{3}$	10	$10^{4}-10^{6}$	$1-10^{2}$	0.937	0−10	Dragon skin, nylon DuraForm PA	Maximum impact angle at elastic sphere skipping: $\beta_{OEM} \approx 47°$
This article; hydrogel sphere	$10-10^{3}$	1−10	$10^{2}-10^{4}$	$10-10^{3}$	1.003	0–20	23.6°	Rebounding when elastocapillary Mach number $Me > 10$, the ratio of oscillation time to inertial time $\tau_w/\tau_c > 1$ and the ratio of cavity collapse time to inertial time $\tau_p/\tau_c > 5$

Table 3. Dimensionless quantities of various water entry behaviours are summarised based on relevant studies and the results presented in this study.

Mach number Me, related to Y, is introduced through energy partitioning analysis in § 4.1, with the corresponding values included in table 3.

3. Dynamic process of hydrogel sphere water entry

For the motion of the hydrogel sphere impacting liquid at different parameters, we have observed three distinct regimes as shown in figure 3 and Supplementary Movies. Figure 3(*a*) and Supplementary Movie 1 captures a hydrogel sphere ($Y = 150$ Pa, $U_0 = 1.5\ \mathrm{m\,s^{-1}}$) impacting a liquid surface. A transient shallow and narrow cavity forms and then collapses as the contact line reaches the apex. The hydrogel sphere continues to sink vertically, which we refer to as 'sinking'. At $U_0 = 2.5\ \mathrm{m\,s^{-1}}$, the hydrogel sphere ($Y = 150$ Pa) undergoes more pronounced deformation during impact, forming a radially wider and deeper cavity. As the cavity retracts, the hydrogel sphere rises and remains suspended near the surface for a long time, even if its density is higher than that of the surrounding liquid. This behaviour is defined as 'suspension', as illustrated in figure 3(*b*) and Supplementary Movie 2. At $U_0 = 4\ \mathrm{m\,s^{-1}}$ (figure 3(*c*) and Supplementary Movie 4), the hydrogel sphere experiences extreme deformation and cavity expansion. As the cavity retracts, the Worthington jet rebounds above the water surface, while the hydrogel sphere remains encapsulated within the jet and ascends with the retracting cavity – a phenomenon termed 'rebounding', in which elastic and hydrodynamic forces sustain partial submersion rather than full detachment.

In these three types of motion, the cavity morphologies observed are classified as the quasi-static seal, following the established categorisation for solid sphere water entry (Aristoff & Bush 2009; Speirs *et al.* 2019). Specifically, for a solid sphere with contact angle of 89°, Speirs *et al.* (2019) reported that cavities transition to the quasi-static seal when $We < 200$ within their investigated Bo range, a behaviour qualitatively similar to our observations. Similarly, previous studies have established $We > 55$ as the critical threshold for Worthington jet formation (Hsiao, Lichter & Quintero 1988), which is consistent with our findings. However, hydrogel spheres may remain submerged even for $We > 55$, indicating that jet formation alone is insufficient to guarantee hydrogel sphere rebound.

We systematically map these parametric dependencies by varying U_0, Y, D_0 and η. Figure 4 presents a phase diagram where colours distinguish different regimes. Notably, all cases experience the transitions of the impact type from 'sinking' to 'suspension' to 'rebounding' regimes as U_0 increases, while the transitions occur at lower U_0 for lower Y. All the data are well classified within these three regimes. The 'rebounding' regime (blue) occurs at high U_0 and low Y, whereas the 'sinking' regime (red) dominates at low U_0 and higher Y, and the 'suspension' regime (grey) lies in between these two regimes for medium U_0 and Y, highlighting the critical role of deformation in the rebound dynamics of hydrogels. Remarkably, for soft hydrogels (low Y), we observe a positive correlation between rebound probability and We – directly opposing the negative We dependence characteristic of solid spheres. It is demonstrated that hydrogel spheres exhibit increased d_m and a higher tendency to rebound with increasing U_0, under fixed values of Y, liquid surface tension σ and density ratio ρ. This behaviour contrasts with that of solid spheres, which are more likely to rebound at lower U_0. Furthermore, rebound is completely suppressed for stiff hydrogels (high Y), such that as hydrogels become stiffer, jet-assisted rebound is absent, similar to the behaviour observed with solid spheres.

This phenomenon is distinct from the mechanism by which the initial jet propels the water strider above the free surface (Watson *et al.* 2024), as it occurs even when $\rho > 1$. To understand these distinct behaviours, we theoretically predict these regime transitions

https://doi.org/10.1017/jfm.2025.10207 Published online by Cambridge University Press

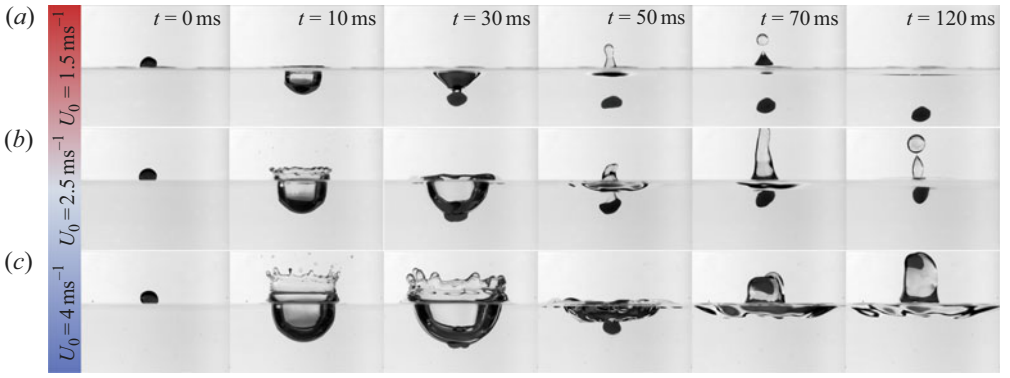


Figure 3. Snapshots of hydrogel sphere impact process at the same $Y = 150$ Pa but three different initial speeds, also representing the three different regimes: (*a*) $U_0 = 1.5$ m s^{-1}, 'sinking' regime; (*b*) $U_0 = 2.5$ m s^{-1}, 'suspension' regime; (*c*) $U_0 = 4$ m s^{-1}, 'rebounding' regime.

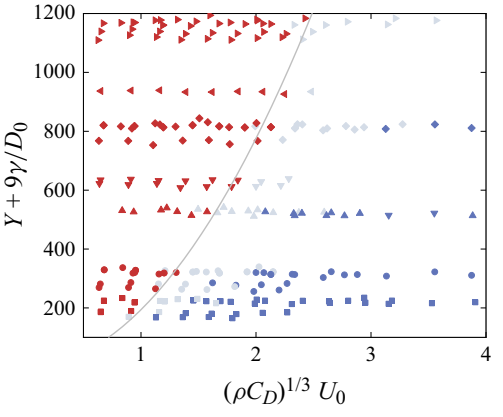


Figure 4. The full phase diagram of all experimental cases in the (U_0, Y) parameter space. The red, grey and blue points represent the cases in the 'sinking', 'suspension' and 'rebounding' regimes, respectively. The solid line represents the prediction curve based on (5.2), derived from a force balance on hydrogel spheres. The vertical axis corresponds to the right-hand side of (5.2), governed by the Young's modulus Y, surface tension γ and diameter D_0 of the hydrogel sphere. The horizontal axis represents the left-hand side of the equation, which depends on the impact velocity U_0, density ratio ρ and drag coefficient C_D, as detailed in the derivation presented in § 5. The data points represent an extended experimental dataset, with corresponding dimensionless parameters in the ranges $Bo \in [1, 10]$ and $We \in [10, 10^3]$, consistent with table 3.

in subsequent sections, revealing the underlying mechanics governing hydrogel impact dynamics.

Starting with the force balance, we consider a sphere impacting a free surface with contact line C and a wetted contact area S_b. The instantaneous force $\mathbf{F}$ acting on the object, composed of hydrodynamic stress and the force generated by surface tension, can be expressed precisely as

$$\mathbf{F} = \int_{S_b} \mathbf{S_T} \cdot \mathbf{n} \mathrm{d}S + \int_C \sigma \mathbf{t} \mathrm{d}\ell, \tag{3.1}$$

where $\mathbf{n}$ and $\mathbf{t}$ are the unit vectors normal and tangent to the free surface. Hydrodynamic stress is $\mathbf{S_T} = -p\mathbf{I} + 2\mu\mathbf{E}$, where p is the fluid pressure, $\mathbf{I}$ is the identity matrix and $\mathbf{E} = [\nabla\mathbf{u} + (\nabla\mathbf{u})^T]/2$ is the rate of strain tensor. Applying the Stokes theorem, we

https://doi.org/10.1017/jfm.2025.10207 Published online by Cambridge University Press

transform the line integral into an equivalent surface integral over S:

$$\int_C \sigma \mathbf{t} \mathrm{d}\ell = \int_{S_b} [\sigma(\nabla \cdot \mathbf{n})\,\mathbf{n} - \nabla\sigma] \mathrm{d}S. \tag{3.2}$$

The surface tension contributes to both the normal and tangential stresses at the interface. The normal stress is given by the Laplace pressure $\sigma\kappa$, where $\kappa = \nabla \cdot \mathbf{n}$ is the interface curvature. The tangential stress arises from surface tension gradients $\nabla\sigma$. In our experiments, the cavity dynamics is characterised by the maximum depth $H^* = 10^{-3}$ m and its associated time scale $T^* = 10^{-2}$ s. This gives dimensionless numbers $Re = \rho_w H^{*2}/(T^*\eta) \approx 10^4$ and $Ma = H^*/(T^*c) \approx 10^{-4}$, where $c = 1500\ \mathrm{m\,s^{-1}}$ is the speed of sound in water. With $Re \gg 1$ and $Ma \ll 1$, both viscous and compressibility effects are negligible.

For inviscid flow, the pressure p is related to the velocity fields through the unsteady Bernoulli equation: $(\partial\phi/\partial t) + (1/2)|\mathbf{u}|^2 + (p + \rho\mathbf{g}\cdot\mathbf{z})/\rho = Q$. Here, $\mathbf{u}$ is the fluid velocity, ϕ is the velocity potential, $\mathbf{g}$ is gravity, $\mathbf{z}$ is the position of the sphere and Q is a constant. Substituting the Bernoulli pressure p into the hydrodynamic stress tensor $\mathbf{T}$, then the combination of $\mathbf{T}$, curvature force (3.2) and (3.1) yields a force

$$\mathbf{F} = \int_{S_b} \left[\left(\rho_w \frac{\partial\phi}{\partial t} + \tfrac{1}{2}\rho_w |\mathbf{u}|^2 - \rho_w \mathbf{g}\cdot\mathbf{x} + \sigma(\nabla\cdot\mathbf{n}) \right) \right] \mathbf{n} - \int_{S_b} \nabla\sigma\ \mathrm{d}S. \tag{3.3}$$

The integrated form of (3.3) yields the complete force balance comprising five key contributions, including the drag force $\rho_w U^2 A$, buoyancy force $\rho_w g H A$, added mass force $\rho_w V \mathrm{d}U/\mathrm{d}t$, curvature force $\sigma A/L$ and Marangoni force $\nabla\sigma A$. Taking impact velocity U_0, sphere volume D_0^3, contact area D_0^2, contact width D_0 and penetration depth H^* as characteristic scales, the dimensional scaling reveals that inertial forces $\rho_w U_0^2 D_0^2$ dominate at $\mathcal{O}(10^{-2})$, while buoyancy $\rho_w g D_0^3 \sim \mathcal{O}(10^{-3})$, hydrostatic pressure $\rho_w g H^* D_0^2 \sim \mathcal{O}(10^{-5})$ and capillary effect $\sigma D_0^2/L \sim \mathcal{O}(10^{-5})$ are secondary. The added mass $\rho_w D_0^3 U_0/T^* \sim \mathcal{O}(10^{-4})$ becomes negligible during rapid acceleration, and the effect of Marangoni force $\nabla\sigma D_0^2 \sim 0$ remains negligible throughout the impact process. Therefore, the drag force dominates all other contributions by at least one order of magnitude during the initial impact stage ($t \leqslant T^*$). This permits a simplified force balance:

$$\rho_s V \ddot{z}_c = \tfrac{1}{2}\rho_w A U^2 C_D, \tag{3.4}$$

where V is the volume of the sphere, z_c is the displacement of the sphere, U is the centre-of-mass velocity of the sphere, C_D is the drag coefficient and A is the wetted area. Completely understanding the phase diagram requires modelling A, U and C_D via a coupled analysis of hydrogel deformation and cavity dynamics in subsequent sections.

4. Modelling hydrogel deformation and cavity dynamics

The impact dynamics of hydrogel spheres exhibits strong coupling between elastic deformation and cavity evolution. Following the energy-based framework in prior studies of droplet impacts (Chantelot *et al.* 2018) and granular impacts (Ye & Meer 2021), the impact energy is partially used for the deformation of the droplet, and the remaining part may be used for the formation of the crater. We hold the same argument and investigate these phenomena by analysing the energy distribution between sphere deformation and target response to determine the sphere's contact area A and U.

https://doi.org/10.1017/jfm.2025.10207 Published online by Cambridge University Press

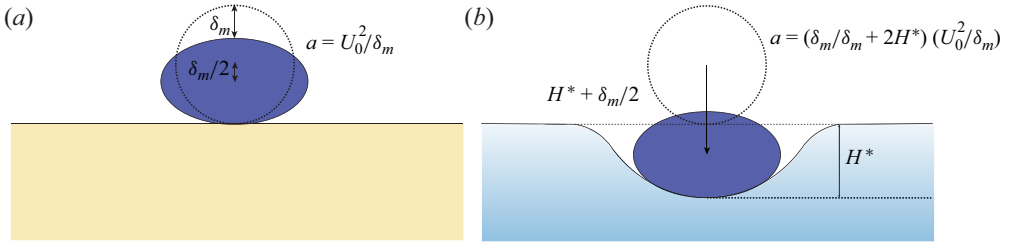


Figure 5. The relevant average deceleration experienced by (*a*) a hydrogel sphere impacting on solid and (*b*) a hydrogel sphere impacting on liquid.

As established in previous work (Ye & Meer 2021), when a hydrogel impacts a solid substrate, the spreading diameter reaches its maximum, producing a centroid displacement of $\delta_m/2$ (figure 5*a*). The solid surface exerts an average force $2E_k/\delta_m$ on the sphere, yielding an average deceleration $a \approx U_0^2/\delta_m$. In our experiments where water replaces the solid substrate (figure 5*b*), the centre-of-mass displacement increases to $\delta_m/2 + H^*$. Consequently, the deceleration is reduced to

$$a = \frac{U_0^2}{\delta_m + 2H^*} = \frac{\delta_m}{\delta_m + 2H^*}\,\frac{U_0^2}{\delta_m}. \tag{4.1}$$

This indicates that, for the same impact kinetic energy, the deceleration of the hydrogel decreases from $a = U_0^2/\delta_m$ to $a = (\delta_m/(\delta_m + 2H^*))U_0^2/\delta_m$, a reduction by a factor of $\xi = \delta_m/(\delta_m + 2H^*)$, which is equivalent to the hydrogel sphere impacting a solid surface with an effective kinetic energy $E_d = \xi E_k$. In other words, when a hydrogel sphere impacts a liquid, the impact kinetic energy E_k is partitioned into two components: E_d, which is used for the deformation of the hydrogel sphere, and $E_s = E_k - E_d$, which is used for the formation of the cavity. These components are defined as follows:

$$E_d = \frac{\delta_m}{\delta_m + 2H^*}E_k \qquad \text{and} \qquad E_s = \frac{2H^*}{\delta_m + 2H^*}E_k. \tag{4.2}$$

We can estimate the maximum vertical deformation δ_m based on the incompressibility condition, given by $\delta_m \approx D_0 - D_0^3/d_m^2$, where d_m represents the maximum deformation diameter of the hydrogel sphere. Notably, when the hydrogel sphere reaches d_m, both the sphere and the surrounding liquid move at identical velocities, inducing the added mass force. The above dimensional analysis indicates that the added mass effects are negligible in comparison with inertial forces.

4.1. *Spreading diameter of hydrogel spheres*

To characterise the evolving morphology of the hydrogel, we employ the digital image correlation technique developed by Zhao *et al.* (2019). In our experimental imaging conditions, the sphere appears as a dark elliptical profile due to the combined effects of viewing perspective and illumination. The instantaneous spreading diameter d is determined by identifying maximum-correlation template size, from which the maximum diameter d_m is extracted through temporal analysis of the impact sequence.

Figure 6(*a*) exhibits the scaled maximum spreading diameter $\lambda_m = d_m/D_0$ versus U_0. The scaled maximum diameter λ_m shows a pronounced increase with both decreasing Y and U_0, revealing the coupled influence of material properties and impact energy on spreading dynamics. Hurd *et al.* (2017) revealed that the peak spreading diameters of the sphere could be predicted using neo-Hookean hyperelasticity, scaled by the

https://doi.org/10.1017/jfm.2025.10207 Published online by Cambridge University Press

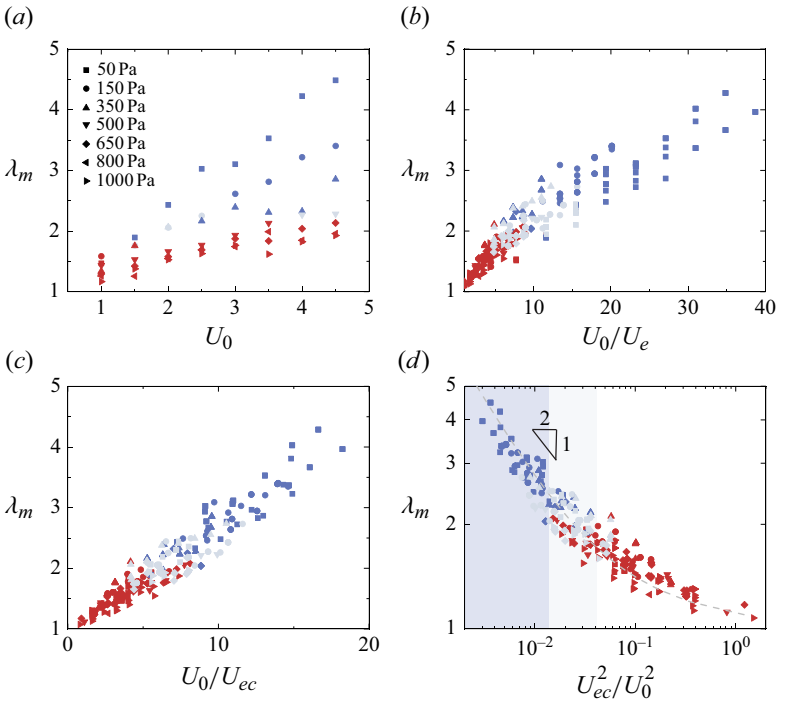


Figure 6. Dimensionless maximum spreading diameter λ_m of hydrogel spheres as a function of: (*a*) impact velocity U_0 for varying Y, (*b*) elastic Mach number U_0/U_e, (*c*) elastocapillary Mach number U_0/U_{ec} and (*d*) inverse square law U_{ec}^2/U_0^2.

dimensionless group $G/\rho_w U_0^2$. Here, G is the shear modulus of the sphere, related to $Y = 2G(1+\nu) \approx 3G$. It is similar to the work of Tanaka, Yamazaki & Okumura (2003), who studied cross-linked gels ($Y \approx 2000$ Pa) impacting non-adhering rigid substrates and applied the balance of inertial and elastic energies to predict maximum spreading diameter. We now extend this energy-balance approach to our system, equating E_e with the portion E_d of the impact kinetic energy that is available for the sphere deformation. Based on elasticity theory, the bulk elastic energy $E_e \approx \pi D_0^3 G(2\lambda_m^2 + \lambda_m^{-4} - 3)/12$. When the maximum spreading diameter is significantly large ($\lambda_m \gg 1$), the first term dominates the elastic energy, leading to $E_e \approx \pi D_0^3 G\lambda_m^2/6$. We derive the expression for the spreading diameter by applying the energy conversion $E_d = E_e$, which gives

$$\lambda_m \approx \frac{\sqrt{\xi}}{\sqrt{2}} \frac{U_0}{U_e}. \tag{4.3}$$

Here, the quantity $\sqrt{\xi}U_0/U_e = \sqrt{\xi}Ma$ can be interpreted as a modified elastic Mach number and $U_e = \sqrt{Y/3\rho_s}$ represents the characteristic velocity of transverse elastic waves. Figure 6(*b*) presents λ_m versus the modified elastic Mach number Ma for an extended dataset including various liquid viscosities and sphere diameters. While the data collapse well at lower values of this parameter, the scaling deteriorates at higher values. This is due to the surface tension term becoming significant (Arora *et al.* 2018; Ye & Meer 2021) when $l_{ec}/D_0 \gtrsim 1$, where $l_{ec} \equiv 9\gamma/Y$ is the elastocapillary length, derived from $G + 3\gamma/D_0 = 3Y(1 + l_{ec}/D_0)$. Given our experimental range of moduli (50–1000 Pa), we introduce the surface energy term $E_c \approx \pi D_0^2 \gamma \lambda_m^2/2$ into the balance. Consequently, the sum of the elastic and capillary energies must be in balance with the portion of

https://doi.org/10.1017/jfm.2025.10207 Published online by Cambridge University Press

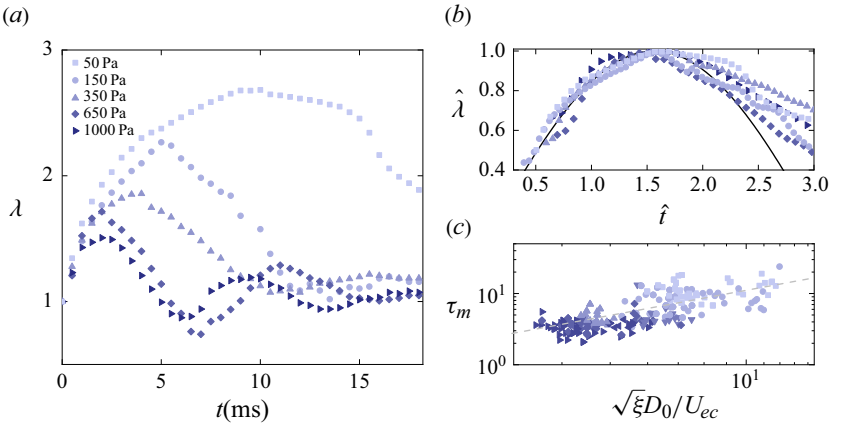


Figure 7. Dimensionless spreading diameter of hydrogel spheres: (*a*) λ versus time and (*b*) $\hat{\lambda} = d/d_m$ versus the dimensionless time $\hat{t} = \omega t$. (*c*) The measured spreading time τ_m versus the theoretical scaling $\sqrt{\xi}\, D_0/U_{ec}$.

the impact kinetic energy available for the deformation of the sphere $\xi\pi\rho_s D_0^3 U_0^2/12 = \pi D_0^3 G\lambda_m^2/6 + \pi D_0^2\gamma\lambda_m^2/2$, which finally gives

$$\lambda_m \approx \frac{\sqrt{\xi}}{\sqrt{2}}\frac{U_0}{U_{ec}} \quad \text{with} \quad U_{ec}^2 = U_e^2 + U_c^2 = \frac{Y}{3\rho_s} + \frac{3\gamma}{\rho_s D_0}. \tag{4.4}$$

Figure 6(*c*) demonstrates the universal scaling of λ_m with the elastocapillary Mach number $M_e = U_0/U_{ec}$ (using $\gamma = 7.3 \times 10^{-2}$ N m^{-1}), where all experimental data collapse onto a single master curve. To contrast with previous scaling laws, we further plot λ_m against U_{ec}^2/U_0^2 in figure 6(*d*) (the dashed line is plotted using the expression for the full curve $\lambda_m^2 = g[(\delta_m/(\delta_m + 2Z_c^*))U_0^2/U_{ec}^2]$, where $g[\dots]$ is the inverse of $f(\lambda_m^2) = 2\lambda_m^2 + \lambda_m^{-4} - 3$). This vertical impact result proves a linear scaling relationship between the maximum spreading ratio λ_m and the Mach number Ma. Building on prior studies, Belden *et al.* (2016) demonstrated a soft sphere (approximately 500 Pa) in obliquely impacting water, showing that for shallow impacts (11.5°), λ_m is approximately proportional to $Ma^{2/3}$, while for deep impacts (47°), λ_m is approximately proportional to $Ma^{5/6}$. The linear relationship reveals critical limit scaling behaviour as the impact angle approaches vertical. It is noted that the rebound of hydrogel spheres occurs in the region defined by $U_{ec}^2/U_0^2 < 10^{-2}$, which represents an extended parameter region that has not been previously investigated.

Turning back to the spreading diameter, we measure the time evolution of the sphere diameter d with varying Y under fixed U_0, as shown in figure 7(*a*). The experimental data capture the spreading behaviour of hydrogel spheres in three types of motion for clarity. All curves exhibit expansion–retraction behaviour, with the time to reach d_m decreasing significantly as Y increases. The spreading dynamics can be treated as that of a one-dimensional harmonic oscillator. The equivalent stiffness coefficient K of the hydrogel sphere is derived by equating the spring potential energy $K\lambda_m^2/2$ to the sum of the elastic and capillary energies. Under the condition $\lambda_m \gg 1$, we obtain

$$K = \frac{\pi}{\xi}\left(\gamma + \frac{G_0 D_0}{3}\right). \tag{4.5}$$

https://doi.org/10.1017/jfm.2025.10207 Published online by Cambridge University Press

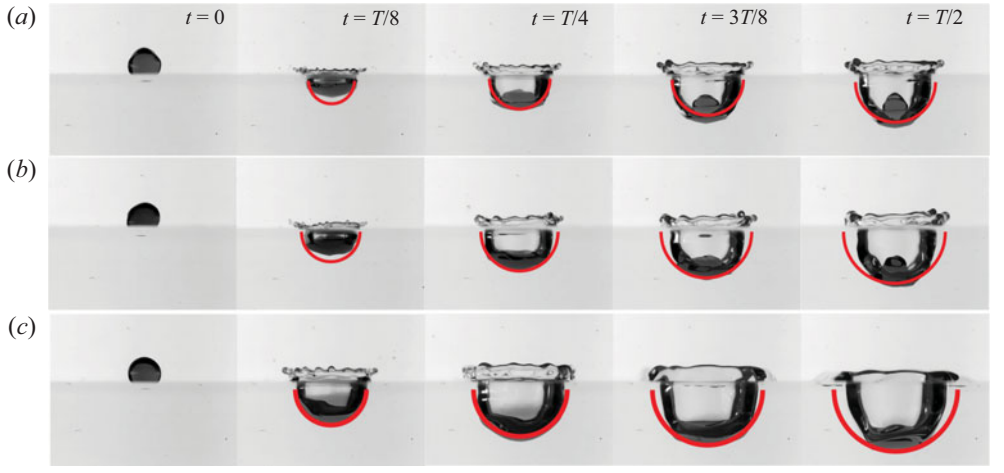


Figure 8. Snapshots from the entry of hydrogel spheres onto water, for three different values of the Young's modulus, namely (*a*) 1000 Pa, (*b*) 350 Pa and (*c*) 50 Pa, for the same impact velocity $U_0 = 2\ \mathrm{m\,s^{-1}}$. The red semicircle represents the cavity profile predicted by potential flow theory. Each row represents five consecutive snapshots of an impact, where the leftmost column illustrates the moment of initial contact between the hydrogel sphere and the liquid, $t = 0$. The subsequent snapshots correspond to $t = T/8$, $t = T/4$, $t = 3T/8$ and $t = T/2$. Here, T is the oscillation period of a hydrogel sphere, that is, $T = 2\pi/\omega = \sqrt{2\xi}\pi D_0/U_{ec}$.

This effective stiffness combines contributions from bulk elasticity and surface tension. From the conservation of total energy $m\dot{\lambda}^2 + K\lambda^2 = K\lambda_m^2$, it can be inferred that at any moment, the normalised spreading and contracting diameter $\lambda = d/D_0$ of the hydrogel sphere is

$$\lambda = \lambda_m \sin(\omega t + \Theta), \tag{4.6}$$

where $\omega = \sqrt{K/m}$ is the oscillation frequency and $\Theta = \arcsin(1/\lambda_m)$ is the initial phase. Equation (4.6) reduces to a dimensionless form $\hat{t}$ when time is normalised by ωt, and $\hat{\lambda} = d/d_m$. Applying the same rescaling to experimental data yields agreement between measurements and theoretical predictions during the first quarter-period, as illustrated in figure 7(*b*). Weak deviations emerge in the subsequent quarter-period during sphere retraction, which originates in viscous dissipation between the hydrogel sphere and surrounding liquid, or inherent viscous dissipation. The temporal evolution of the spreading diameter establishes the foundational framework for calculating the wetted area A.

In addition to the maximum spreading diameter, we quantified the spreading time τ_m, defined as the time interval from the initial impact to the maximal deformation reached, which is plotted in figure 7(*c*). The measured τ_m corresponds to one-quarter of its oscillation period, consistent with the theoretical scaling of the oscillation period $T = 2\pi/\omega = \sqrt{2\xi}\pi D_0/U_{ec}$. The time scale is discussed in § 5.

4.2. *Cavity evolution modelling*

The impact generates an axisymmetric air cavity that expands radially before collapsing. Figure 8 illustrates the cavity evolution in $T/2$ oscillation time for three distinct Y at $U_0 = 2.0\ \mathrm{m\,s^{-1}}$. During cavity expansion, the strong hydrophilic hydrogel promotes coalescence between the sphere's base and the advancing cavity interface, thereby exerting a nearly uniform surface force on the cavity. This leads to the cavity geometry approaching a state where the diameter becomes approximately equal to the depth prior to collapse.

https://doi.org/10.1017/jfm.2025.10207 Published online by Cambridge University Press

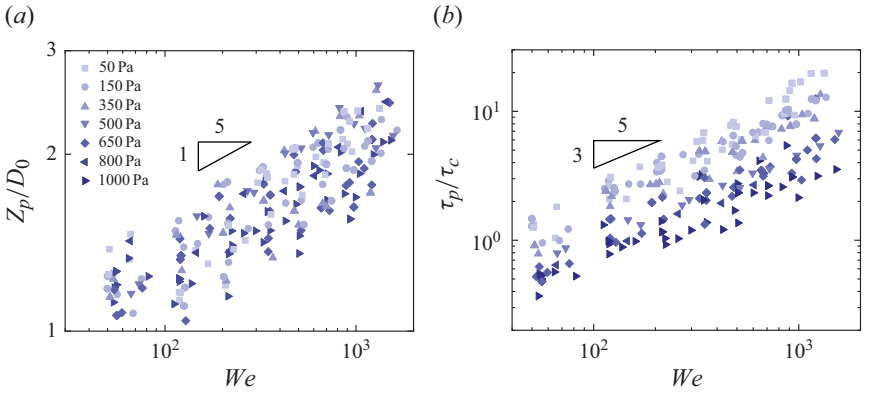


Figure 9. The normalised (*a*) pinch depth Z_p/D_0 and (*b*) pinch time τ_p/τ_c of the cavity are plotted against We for the impact of hydrogel spheres with different Young's moduli Y. The measurement methodology is outlined in Speirs *et al.* (2019).

To systematically investigate the interplay between hydrogel dynamics and cavity collapse, we quantify the pinch-off depth Z_p and pinch-off time τ_p of the cavity using the methodology outlined in Speirs *et al.* (2019). Here, Z_p is defined as the distance from the undisturbed free surface to the location where the cavity walls collapse, while τ_p represents the time from impact to the pinch-off event. In the quasi-static regime of the cavity, Z_p increases with the Weber number We, while remaining bounded below $3D_0$. All values of Z_p resulting from impacts on cavities with varying Y lie within this range, demonstrating a remarkable insensitivity to elasticity, as illustrated in figure 9(*a*). The observed spread in Z_p originates from the combined effects of initial conditions, including Y, D_0, U_0 and η. While, the normalised pinch-off time τ_p/τ_c (where τ_c is derived in § 5) reveals a more complex dependence, exhibiting exponential growth with We while maintaining distinct stratification by Y. These observations highlight the dominant role of Me in governing cavity collapse dynamics, particularly in the formation of nested matryoshka cavities, which are related to sphere rebound. The complete explanation of these coupled phenomena is developed in § 5.

Now, we proceed by developing a theoretical description of the cavity evolution. As mentioned in § 3, the pressure is related to the velocity field through the unsteady Bernoulli equation $(\partial\phi/\partial t) + (1/2)|\mathbf{u}|^2 + (p + \rho_w \mathbf{g}\cdot\mathbf{z})/\rho_w = Q$ for inviscid flow. For any point A within the cavity at an arbitrary moment, and any point B at the initial moment, as plotted in figure 1(*c*), integrating the Bernoulli equation yields the following result:

$$\left[\frac{\partial\phi}{\partial t} + \frac{|\mathbf{u}|^2}{2} + \frac{p + \rho_w \mathbf{g}\cdot\mathbf{z}}{\rho_w}\right]_A^B = 0. \tag{4.7}$$

At the free surface, the conditions $\mathbf{u}_B = 0$ and $\mathbf{z}_B = 0$ are satisfied. Additionally, according to the inequality of pressures across the liquid interface, as described by the Young–Laplace equation, it follows that $p_A - p_B = 2\gamma/R$, where $R(\theta, t)$ represents the radius determining the location of the interface at time t in the direction θ. Hence, (4.7) takes the form

$$\rho_w \frac{\partial\phi}{\partial t}|_A + \rho_w \frac{|\mathbf{u}_A|^2}{2} + \rho_w g z_A + \frac{2\gamma}{R} = 0. \tag{4.8}$$

https://doi.org/10.1017/jfm.2025.10207 Published online by Cambridge University Press

Initially, the cavity exhibits isotropy with $\partial/\partial r \gg \partial/\partial\theta$, and $\partial/\partial z = 0$. Mass conservation implies $\partial(r^2 u_r)/\partial r = 0$, which yields $u_r = (R/r)^2\dot{R}$ and $\phi(r, t) = -R^2\dot{R}/r$. Incorporating these equations into the differential equation governing cavity dynamics, derived from (4.8):

$$R\ddot{R} + \frac{3}{2}\dot{R}^2 + gR\sin\theta + \frac{2\gamma}{\rho R} = 0. \tag{4.9}$$

By integrating the aforementioned equation, we obtain

$$\rho R^3\dot{R}^2 + \frac{1}{2}\rho_w g R^4 \sin\theta + 2\gamma R^2 = E_0. \tag{4.10}$$

In this formulation, E_0 represents the integration constant, typically determined by the initial condition $\dot{R}(t = 0)$. For solid water entry problems, when the sphere's motion is decoupled from cavity evolution, $\dot{R}(t = 0) = 0$ is used (Duclaux *et al.* 2007). However, when the interaction between sphere dynamics and the cavity is coupled (Aristoff & Bush 2009; Aristoff *et al.* 2010), the instantaneous velocity of the sphere is generally required. In our case, the energy allocated to cavity evolution is E_s, as described in § 4, thereby defining the integration constant as $E_0 = E_s$. Additionally, taking Z_p as the characteristic length scale, scaling arguments demonstrate that gravitational potential and surface tension energies are negligible. This simplification yields $R^3\dot{R}^2 = E_s/\rho_w$, leading to

$$R(t) = \left(\frac{5}{2}\sqrt{\frac{E_s}{\rho_w}}t\right)^{2/5}. \tag{4.11}$$

A similar power law with t for cavity evolution was derived in previous studies (Taylor 1950; Duclaux *et al.* 2007; Aristoff & Bush 2009; Benusiglio, Quéré & Clanet 2014).

Figure 10(*a*,*b*) illustrates the temporal evolution of cavity radius R and velocity $\dot{R}$ for varying U_0. Further analysis of figure 10(*a*) in log–log coordinates reveals a characteristic slope of 2/5, confirming the universal scaling $R \propto t^{2/5}$, as shown in figure 10(*b*). To generalise these results, we normalise the cavity radius as $\hat{R} = R/(5/2\sqrt{E_s/\rho_w})^{2/5}$. Remarkably, this normalisation collapses all data spanning diverse Y, U_0 and D_0 onto a single $t^{2/5}$ master curve. These results provide the expression of $\dot{R}$ required to model the hydrodynamic forces.

5. Prediction of regime transition

Rebounding of the hydrogel sphere is a counterintuitive phenomenon for vertical water impact since $\rho > 1$. While solid sphere water entry typically involves superhydrophobic surfaces, hydrophilic spheres with a contact angle $\sim 90°$ require $We < 1$ and $Bo < 0.5$ for rebound (Speirs *et al.* 2019). Recent numerical and experimental studies on skipping and rebounding of deformable spheres reveal that elastic deformation energy increases the critical rebound angle to 47°, demonstrating that traditional parameters, such as We, Bo and wettability, cannot fully predict rebound dynamics alone (Belden *et al.* 2016). This necessitates the introduction of new dimensionless groups Ma or Me to characterise the role of deformability in phase space.

Theoretically, vertical rebound becomes feasible when the sphere's shear modulus satisfies $G \approx \gamma/D_0$. For a 4 mm sphere with density ratio $\rho = 1$, this criterion requires shear modulus $G < 20$ Pa. Our experiments demonstrate that even hydrophilic hydrogel spheres with $G \sim 100$ Pa still achieve vertical rebound. To understand the mechanism behind this, we revisit the force balance (3.4) governing sphere dynamics during impact.

https://doi.org/10.1017/jfm.2025.10207 Published online by Cambridge University Press

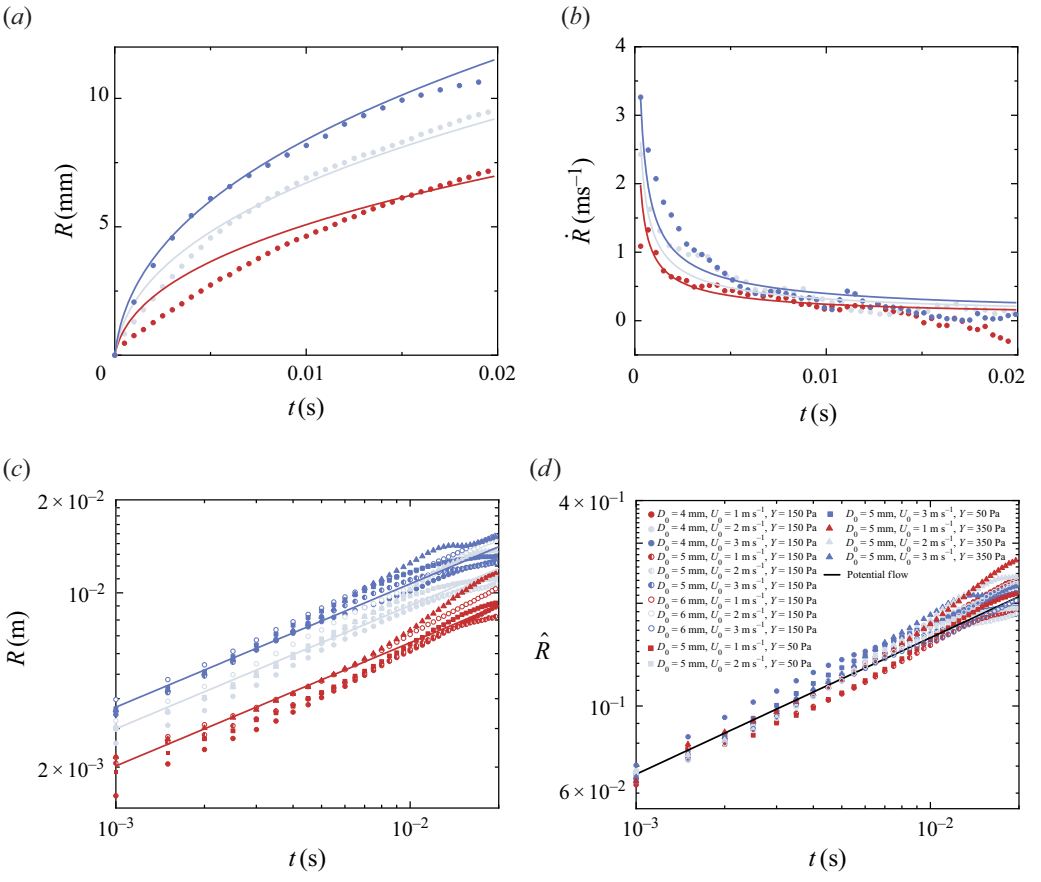


Figure 10. The evolution of (*a*) the cavity radius R and (*b*) the velocity at the bottom of the cavity $\dot{R}$, (*c*) log–log plot of the cavity radius R and (*d*) normalised cavity radius $\hat{R}$ plotted versus time. The circles represent experimental results and the solid lines are the theoretical predictions by $R = (5/2\sqrt{E_s/\rho_w}t)^{2/5}$ in (*a*), $U = \dot{R}$ in (*b*) and $\hat{R} = R/(5/2\sqrt{E_s/\rho_w})^{2/5}$ in (*d*). Note that the extended dataset has been included in (*c*,*d*), and the same symbols legend of (*d*) is shared by the other panels.

With measured λ, integrating over T yields the equivalent wetted area $A = \pi\bar{\lambda}^2/4 = \pi(\int_0^{T/2}\lambda \mathrm{d}t/T)^2 = (1/\pi)D_0^2\lambda_m^2$. Additionally, the centroid velocity of sphere U converges to the cavity evolution rate $\dot{R}$ when the velocity difference induced by hydrogel deformation is negligible, given by $U = 2/5(5/2\sqrt{E_s/\rho_w})^{2/5}t^{-3/5}$. The last piece is the drag coefficient C_D, as determined by $C_D = 18.5/Re^{0.5}$ (MotMottt, Noor & Aziz 2006), considering that Re ranges from 2.4×10^2 to 2.5×10^4 in our experiment.

Based on the analysis by Hurd *et al.* (2017), we also define the characteristic acceleration as $(U_2 - U_0)/T = \Delta U/T$, where U_2 represents the velocity of the sphere's centre of mass after one oscillation period. Substituting these physical quantities back into (3.4), the velocity difference after a completed oscillation period can be obtained by integrating (3.4) over T. This allows us to reformulate as

$$\frac{U_0 - U_2}{U_0} = \frac{3\sqrt{2}}{32}\rho C_D \xi^{3/2} Me^3. \tag{5.1}$$

https://doi.org/10.1017/jfm.2025.10207 Published online by Cambridge University Press

The critical rebound occurs at $U_2 = 0$. Having pieced all the puzzles together, we can derive the critical transition curve (Y, U_0) for sinking and suspension:

$$Y + 9\gamma/D_0 = a_1 \left(\frac{C_D}{\rho}\right)^{2/3} U_0^2, \tag{5.2}$$

where $a_1 = 3(3\sqrt{2}/32)^{2/3}\rho_s\xi$. The final theoretical curve from (5.2) is shown in figure 4, which qualitatively captures all experimental observations and successfully predicts the transition from 'sinking' to 'suspension'.

Let U_{min} denote the minimum critical impact velocity required to suspend the sphere, which is determined by solving the critical motion equation (5.2). Given measurable properties of the hydrogel sphere and fluid, this equation yields the critical impact velocity U_0, which corresponds to U_{min}. In the limiting analysis of Belden *et al.* (2016), U_{min} for horizontal impacts follows a lower bound proportional to $Y^{1/5}$. In contrast, for deep impacts at an angle of 47°, U_{min} scales with $Y^{5/22}$. Our experimental and theoretical results provide insight into the critical upper bound for the rebound of an elastic sphere during vertical water entry, suggesting that U_{min} in this case is related to $Y^{1/2}$. Given that U_{min} is the characteristic velocity and $2D_0/\tau_c^2$ is the characteristic acceleration, (3.4) can be estimated as

$$\frac{2D_0}{\tau_c^2} \approx \frac{3C_D U_0^2 \lambda_m^2}{\pi^2 D_0 \rho}. \tag{5.3}$$

Therefore, the inertial time scale is given by $\tau_c = (\pi D_0/U_0\lambda_m)\sqrt{2\rho/3C_D}$. The oscillation time of the sphere is given by $\tau_w = \pi/2\sqrt{K/\rho_s V} = (\sqrt{\xi}\pi D_0)/(2\sqrt{2}U_{ec})$. The ratio between them is

$$\frac{\tau_w}{\tau_c} = \frac{\xi}{4}\sqrt{\frac{3C_D}{2\rho}}\frac{U_0^2}{U_{ec}^2}. \tag{5.4}$$

Equation (5.4) exhibits that the time-scale ratio is related to $(U_0/U_{ec})^2$. Belden *et al.* (2016) proposed that the critical time scale is $\tau_w/\tau_c \sim U_0/U_{ec}$ for a shallow impact angle, and $\tau_w/\tau_c \sim (U_0/U_{ec})^{11/6}$ for a steep impact angle of 47°. Our results, once again, reveal an upper bound, given by $\tau_w/\tau_c \sim (U_0/U_{ec})^2$. The experimental and theoretical results, as shown in figure 11, explain the rebounding mechanism in the vertical water entry.

More significantly, our observations indicate that the ratio of the spreading time to the impact duration is a critical parameter that determines whether sinking occurs. Returning to the spreading time τ_m presented in figure 7(*c*), we compare the measured τ_m with the theoretical oscillation time τ_w for a hydrogel sphere with varying Y, which is equal to one-quarter of the oscillation period of the hydrogel sphere.

The dimensionless ratio τ_w/τ_c exhibits a linear correlation across all experimental data. A distinct threshold emerges at $\tau_w/\tau_c \approx 1$, indicated by a horizontal dashed line, which separates sinking and suspension, as shown in figure 11(*a*). Here, τ_w characterises the horizontal spreading time scale, while τ_c represents the vertical motion time scale (Richard & Quéré 2000). When $\tau_w > \tau_c$, the impact energy predominantly converts into horizontal oscillations, excluding rebound behaviour. Furthermore, τ_w corresponds to the time required for circumferential elastic waves to propagate to the air–water interface. The matryoshka phenomenon manifests when the total contact time τ_c exceeds this wave propagation time τ_w (Belden *et al.* 2016). In this case, sphere vibrations interact with water through the matryoshka cavity, significantly decreasing bouncing efficiency.

https://doi.org/10.1017/jfm.2025.10207 Published online by Cambridge University Press

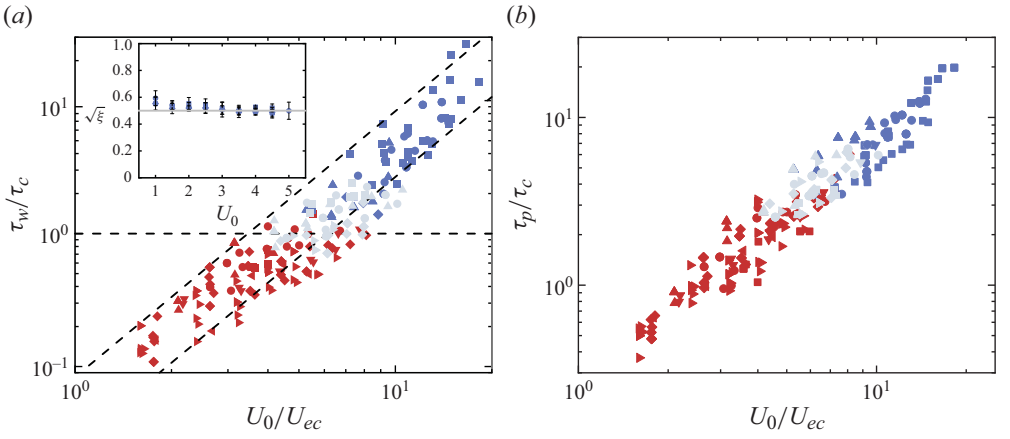


Figure 11. Ratio of the (*a*) sphere oscillation time $\tau_w = \sqrt{\xi}\pi D_0/(2\sqrt{2}U_{ec})$ to inertial time $\tau_c = (\pi D_0/U_0\lambda_m)\sqrt{2\rho/3C_D}$ and (*b*) cavity pinch time τ_p to sphere inertial time τ_c versus the elastocapillary Mach number U_0/U_{ec}. Note that the extended dataset from figure 9 has been used to create this plot, using the same symbols. The symbols denote experimentally measured ratios of (*a*) sphere spreading time τ_m (with τ_m values extracted from figure 7*c*) and (*b*) cavity pinch time τ_p to τ_c (where τ_p data are taken from figure 9*b*). In (*a*), the dashed lines delineate the theoretical bounds for the drag coefficient C_D, encompassing variations in D_0, U_0 and η. The inset of (*a*) shows $\sqrt{\xi}$ as a function of U_0.

Regarding the dimensionless ratio τ_p/τ_c, as shown in figure 11(*b*), rebound becomes possible only when $\tau_c \approx \tau_p$ (Aristoff *et al.* 2010) in solid sphere entry, indicating strong coupling between sphere dynamics and cavity evolution. Our vertical impact experiments demonstrate that $\tau_p/\tau_c = 5$ serves as the critical threshold separating sinking and suspension regimes. Both oscillation time and cavity collapse time effectively characterise the liquid response, with these critical ratios highlighting the strongly coupled nature of hydrogel–liquid interactions.

We further plot $\sqrt{\xi}$ as a function of U_0 in figure 11(*a*) for different diameters, which shows that ξ is nearly constant with increasing impact velocity as the prefactor in (5.2), as well as in the energy distribution relation. Interestingly, it shows that the distribution of initial kinetic energy to the surface energy is a constant value regardless of the control parameters, and this conclusion can be potentially extended to other impact problems with deformable projectiles.

6. Conclusion

In this study, we have introduced and characterised an intriguing rebounding phenomenon observed during the vertical water entry of highly deformable hydrogel spheres. This behaviour contrasts with the well-known sinking of rigid or weakly deformable solids and persists even when the density of the hydrogel sphere exceeds that of water. Through systematic experiments and theoretical modelling, we demonstrated that the elastic deformations at the sphere–liquid interface oscillate and inject extra energy that drives the unexpected rebound. Our high-speed imaging captured the complete sequence of events – from initial impact to maximum spreading, cavity formation and eventual rebound. These observations allowed us to quantify the spreading area, cavity depth and deformation dynamics over time. Analysis of the energy distribution revealed that the interplay between elastic energy storage and hydrodynamic drag governs the fate of the sphere after impact.

https://doi.org/10.1017/jfm.2025.10207 Published online by Cambridge University Press

We showed that the spreading diameter evolves analogously to a one-dimensional harmonic oscillator, driven by impact-induced elastic compression and subsequent recovery. In parallel, the cavity depth evolution follows a potential flow framework, similar to classical water entry problems. Combining these perspectives, we developed a predictive model that provides an expression for Y as a function of the impact velocity U_0, identifying the transition boundary between the 'sinking' and 'rebounding' regimes. These results highlighted the crucial role of soft material elasticity in controlling water entry results. In particular, the ability to store and release strain energy within a highly deformable sphere offers a mechanical template for energetic activation at fluid interfaces.

From a broader perspective, our energy-based framework could be extended to account for surface tension effects, viscoelasticity and wetting properties. Future studies could generalise these insights to more complex soft materials, such as gels with anisotropic stiffness, liquid-filled capsules or soft composites. Moreover, exploring oblique impacts, structured surfaces and multi-sphere interactions could further enrich our understanding of soft matter dynamics at fluid interfaces, with implications for environmental processes, biological propulsion and next-generation soft materials design.

Supplementary movies. Supplementary movies are available at https://doi.org/10.1017/jfm.2025.10207.

Acknowledgements. X.Y. wishes to thank X. Zheng, D. van der Meer and J. Zhang for their invaluable support and help.

Funding. The authors acknowledge the financial support of the National Natural Science Foundation of China (nos. 12172156, 12472411, 11872029), National Key R&D Program of China (no. 2023YFF0717200), Ministry of Education and the Fundamental Research Funds for the Central Universities (lzujbky-2024–0y09).

Declaration of interests. The authors report no conflict of interest.

References

Aristoff, J.M. & Bush, J.W. 2009 Water entry of small hydrophobic spheres. *J. Fluid Mech.* **619**, 45–78.

Aristoff, J.M., Truscott, T.T., Techet, A.H. & Bush, J.W. 2010 The water entry of decelerating spheres. *Phys. Fluids* **22** (3), 032102.

Arora, S., Fromental, J.M., Mora, S., Phou, T., Ramos, L. & Ligoure, C. 2018 Impact of beads and drops on a repellent solid surface: a unified description. *Phys. Rev. Lett.* **120** (14), 148003.

Belden, J., Hurd, R.C., Jandron, M.A., Bower, A.F. & Truscott, T.T. 2016 Elastic spheres can walk on water. *Nat. Commun.* **7** (1), 10551.

Benusiglio, A., Quéré, D. & Clanet, C. 2014 Explosions at the water surface. *J. Fluid Mech.* **752**, 123–139.

Bush, J.W. & Hu, D.L. 2006 Walking on water: biolocomotion at the interface. *Annu. Rev. Fluid Mech.* **38** (1), 339–369.

Chantelot, P., Coux, M., Clanet, C. & Quéré, D. 2018 Drop trampoline. *Europhys. Lett.* **124** (2), 24003.

Cheng, N.-S. 2008 Formula for the viscosity of a glycerol- water mixture. *Ind. Engng Chem. Res.* **47** (9), 3285–3288.

Duclaux, V., Caillé, F., Duez, C., Ybert, C., Bocquet, L. & Clanet, C. 2007 Dynamics of transient cavities. *J. Fluid Mech.* **591**, 1–19.

Gilet, T. & Bush, J.W. 2012 Droplets bouncing on a wet, inclined surface. *Phys. Fluids* **24** (12), 122103.

Glasheen, J. & McMahon, T. 1996 A hydrodynamic model of locomotion in the basilisk lizard. *Nature* **380** (6572), 340–342.

Halswell, P., Wilson, P., Taunton, D. & Austen, S. 2012 Hydroelastic inflatable boats: relevant literature and new design considerations. *Intl J. Small Craft Technol.* **154**, B39.

Hsiao, M., Lichter, S. & Quintero, L.G. 1988 The critical weber number for vortex and jet formation for drops impinging on a liquid pool. *Phys. Fluids* **31** (12), 3560–3562.

Hurd, R.C., Belden, J., Jandron, M.A., Fanning, D.T., Bower, A.F. & Truscott, T.T. 2017 Water entry of deformable spheres. *J. Fluid Mech.* **824**, 912–930.

https://doi.org/10.1017/jfm.2025.10207 Published online by Cambridge University Press

KOROBKIN, A. & PUKHNACHOV, V. 1988 Initial stage of water impact. *Annu. Rev. Fluid Mech.* **20** (1), 159–185.
KUBOTA, Y. & MOCHIZUKI, O. 2015 Splash formation due to a frog diving into water. *World J. Mech.* **5** (07), 129–137.
LEE, D.-G. & KIM, H.-Y. 2008 Impact of a superhydrophobic sphere onto water. *Langmuir* **24** (1), 142–145.
LHUISSIER, H., SUN, C., PROSPERETTI, A. & LOHSE, D. 2013 Drop fragmentation at impact onto a bath of an immiscible liquid. *Phys. Rev. Lett.* **110** (26), 264503.
LOHSE, D., BERGMANN, R., MIKKELSEN, R., ZEILSTRA, C., VAN DER MEER, D., VERSLUIS, M., VAN DER WEELE, K., VAN DER HOEF, M. & KUIPERS, H. 2004 Impact on soft sand: void collapse and jet formation. *Phys. Rev. Lett.* **93** (19), 198003.
MOTMOTTT, R.L., NOOR, F.M. & AZIZ, A.A. 2006 *Applied fluid mechanics*.
RABBI, R., KIYAMA, A., ALLEN, J.S. & TRUSCOTT, T. 2022 Droplet lift-off from hydrophobic surfaces from impact with soft-hydrogel spheres. *Commun. Phys.* **5** (1), 331.
RICHARD, D. & QUÉRÉ, D. 2000 Bouncing water drops. *Europhys. Lett.* **50** (6), 769–775.
RICHARDSON, E.G. 1948 The impact of a solid on a liquid surface. *Proc. Phys. Soc.* **61** (4), 352–367.
SHARMA, V., NAND, S., PRAMANIK, S., CHEN, C.-Y. & MISHRA, M. 2020 Control of radial miscible viscous fingering. *J. Fluid Mech.* **884**, A16.
SPEIRS, N.B., MANSOOR, M.M., BELDEN, J. & TRUSCOTT, T.T. 2019 Water entry of spheres with various contact angles. *J. Fluid Mech.* **862**, R3.
TAKAMURA, K., FISCHER, H. & MORROW, N.R. 2012 Physical properties of aqueous glycerol solutions. *J. Petrol. Sci. Engng* **98**, 50–60.
TANAKA, Y., YAMAZAKI, Y. & OKUMURA, K. 2003 Bouncing gel balls: impact of soft gels onto rigid surface. *Europhys. Lett.* **63** (1), 146–152.
TAYLOR, G.I. 1950 The formation of a blast wave by a very intense explosion. - II. The atomic explosion of 1945. *Proc. R. Soc. Lond. A: Math. Phys. Sci.* **201** (1065), 175–186.
TRAN, T., DE MALEPRADE, H., SUN, C. & LOHSE, D. 2013 Air entrainment during impact of droplets on liquid surfaces. *J. Fluid Mech.* **726**, R3.
TRUSCOTT, T.T., EPPS, B.P. & BELDEN, J. 2014 Water entry of projectiles. *Annu. Rev. Fluid Mech.* **46** (1), 355–378.
VELLA, D., LEE, D.-G. & KIM, H.-Y. 2006 The load supported by small floating objects. *Langmuir* **22** (14), 5979–5981.
VELLA, D. & METCALFE, P.D. 2007 Surface tension dominated impact. *Phys. Fluids* **19** (7), 072108.
WATSON, D.A., THORNTON, M.R., KHAN, H.A., DIAMCO, R.C., YILMAZ-AYDIN, D. & DICKERSON, A.K. 2024 Water striders are impervious to raindrop collision forces and submerged by collapsing craters. *Proc. Natl Acad. Sci. USA* **121** (5), e2315667121.
WU, S. & SHANKS, R. 2004 Solubility study of polyacrylamide in polar solvents. *J. Appl. Polym. Sci.* **93** (3), 1493–1499.
YE, X. & MEER, D.V.D. 2021 Hydrogel sphere impact cratering, spreading and bouncing on granular media. *J. Fluid Mech.* **929**, A24.
ZHAO, H., BRUNSVOLD, A. & MUNKEJORD, S.T. 2011 Transition between coalescence and bouncing of droplets on a deep liquid pool. *Intl J. Multiphase Flow* **37** (9), 1109–1119.
ZHAO, S.-C., DE JONG, R. & VAN DER MEER, D. 2019 Formation of a hidden cavity below droplets impacting on a granular substrate. *J. Fluid Mech.* **880**, 59–72.

https://doi.org/10.1017/jfm.2025.10207 Published online by Cambridge University Press